ORIGINAL PAPER

How the projection domains of NF-L and α-internexin determine the conformations of NF-M and NF-H in neurofilaments

F. A. M. Leermakers · E. B. Zhulina

Abstract Making use of a numerical self-consistent field method and polymer brush concepts, we model the solvated corona of neurofilaments (NF) composed of projection domains (unstructured tails) of constituent proteins. Projections are modeled with amino acid resolution. We focus on the importance of the two shortest ones (α-internexin and NF-L) in regulating the conformations of the two longer ones (NF-M and NF-H) in an isolated NF. We take the wild-type NF with no α-internexin as the reference, for which the phosphorylation-induced translocation of M- and H-tails has been examined previously. We demonstrate that a subbrush of L-tails creates an electrostatic potential profile with an approximately parabolic shape. An experimentally relevant (2:1) ratio of L- to α-projections reduces the charge density of the L subbrush and shifts the translocation transition of the H-tails to slightly higher degrees of phosphorylation. Replacing all L-tails by α-projections destroys the substructure of the NF corona and this alters the NF response to the phosphorylation of long tails.

Keywords Brush model · Self-consistent field model · Phosphorylation-induced translocation · Subbrush formed by short projections · Flower conformation of long projections · Parabolic electrostatic potential

F. A. M. Leermakers (✉)
Laboratory of Physical Chemistry and Colloid Science,
Wageningen University, Dreijenplein 6,
6307 HB Wageningen, The Netherlands
e-mail: frans.leermakers@wur.nl

E. B. Zhulina
Institute of Macromolecular Compounds of the Russian
Academy of Sciences, 199004 St. Petersburg, Russia

Introduction

Advances in computer simulations and field-theoretical methods present new opportunities to model the structure of biopolymers and of their assemblies. Molecular dynamics and Monte Carlo (MC) simulations can provide deep insights into the behavior of such macromolecular assemblies and relate these to the chemical details of their constituents, e.g., proteins (Mitsutake et al. 2001). However, the applicability of these techniques is typically restricted to relatively short fragments (Luchko et al. 2008; Sorin and Pande 2005). The investigation of larger systems involves a coarse-graining approach, often combined with the theoretical machinery developed for synthetic polymers. Such coarse-grained models were designed to simulate, e.g., aggrecan, a complex polysaccharide–protein association in articular cartilage of synovial joints (Bathe et al. 2005; Nap and Szleifer 2008). Recently, we have applied the self-consistent field model of Scheutjens and Fleer (SF-SCF) (Zhulina and Leermakers 2007a, b, 2010; Leermakers and Zhulina 2008) to probe the structure of neurofilaments (NFs), worm-like protein aggregates with a dense rigid core and an unstructured solvated corona. Together with microtubules, actin, and cross-linking proteins, NFs provide a scaffold that resists mechanical stresses in neuronal cell (Fuchs and Cleveland 1998). NFs have a relatively large persistence length of $l_p \sim 480$ nm (Janmey et al. 2003) and align almost parallel in axons of neurons (Hisanaga et al. 1988).

Early experiments have shown that neurofilaments are composed of three subunit proteins named according to their molecular weight, namely NF-L (light), NF-M (medium), and NF-H (heavy) (Hoffmann and Lasek 1975; Liem et al. 1978). Recent studies (Yuan et al. 2006), however, indicated that α-internexin, a protein shorter in

size than the NF-L, could be a fourth neurofilament component in mature small-caliber axons (Fig. 1).

Self-assembly of NFs is rather different from that of classical association colloids, e.g., micelles formed by surfactants or amphiphilic block copolymers. In the latter case, the cylindrical geometry is one of the possible self-association types that are found at a proper balance between the driving force(s) favoring a solvent-free core and the stopping mechanism(s) in a solvated corona. In contrast, the aggregation of NF proteins is thought to be dictated by packing of the rigid domains, stopped by packing frustrations near the core (Herrmann and Aebi 2004), rather than by repulsive forces that exist in the NF corona.

It is well documented that the NF-L protein is required for proper assembly of neurofilaments (Lee et al. 1993; Hisanaga et al. 1990). NF-L chains are shown to form heterodimers with NF-H and NF-M chains by coiled-coil association with approximately 310 amino acid (aa) residues at the N-termini. These rigid domains then further assemble via protofilaments until a core is formed with 32 chains in its cross-section. Meanwhile, the C-termini, known as the projection domains of the NF proteins, are effectively grafted to the core at separations of 2–3 nm. In human NFs the typical protein composition in terms of number of proteins is L:M:H = 7:3:2 (Janmey et al. 2003), and the numbers of amino acid (aa) residues in the projection domains are $N_H = 607$, $N_M = 504$, and $N_L = 142$ (Human Intermediate Database, http://www.interfil.org). All tails contain a large number of basic and acidic aa residues that are ionized at physiological pH ~ 7. The short
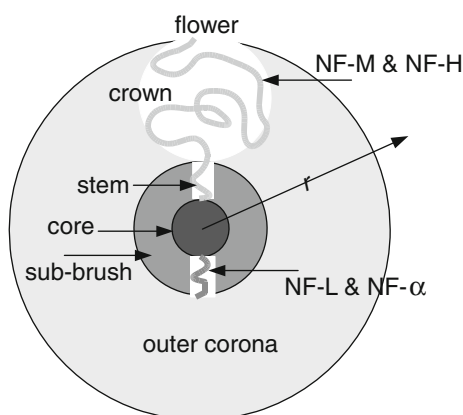

Fig. 1 Schematic illustration of a cross-section through a cylindrical neurofilament brush composed of a cylindrical core and the corona composed of a subbrush and an outer corona. The subbrush is composed of the shorter projections NF-L and NF-α. The longer NF-M and NF-H projections are expelled to the outer brush (especially at high levels of phosphorylation) and assume a flower conformation (when a sufficient number of NF-L is present). The stem and the crown of the flower conformation are indicated. The radial r coordinate is shown as well

L- and the intermediate M-tails are overall negatively charged with an excess number of charges of $\Delta Q_L \approx 35$ and $\Delta Q_M \approx 52$, whereas the long H-tail is a gradient polyampholyte with one excess negative charge $\Delta Q_H = 1$. The H-tail contains, however, about 40 lysine-serine-proline (KSP) motifs, in which serine can be enzymatically phosphorylated to acquire a $-2e$ charge due to the attachment of a phosphate group. KSP motifs are located in the central domain of the H-tail, while its terminal part (abbreviated as the KEP domain) is overall positively charged (Janmey et al. 2003). The M-tail also contains a number of KSP motifs. Referring once again to Fig. 1 for a schematic illustration, the high grafting density of the relatively long projections justifies the picture that the corona is like a cylindrical polymer brush with a quenched number of projections per unit length (Brown and Hoh 1997; Mukhopadhyay et al. 2004; Kumar et al. 2002). This number hardly changes when the forces in the corona vary, e.g., when enzymatic phosphorylation triggers a major conformational transition in the corona or when corona chains form cross-bridges to make the NF network.

Whereas the long M- and H-projections (tails) are routinely seen on electron micrographs (EMs), unambiguous visualization of the L-projection is rare. As a result, to date it even remains debated whether the L-tails reside inside or outside the NF backbone. Atomic force microscopy (AFM) probed a long-range force attributed to the M- and H-projections that sit on the outside of the NF core, but failed to detect a similar force from the reconstituted filaments of NF-L proteins (Brown and Hoh 1997). According to EM images of native and reassembled NFs (Mulligan et al. 1991), however, the L-tails exit from the NF core in the same way as the M- and H-tails do. Small-angle X-ray scattering (SAXS) in solutions of reconstituted filaments composed of NF-L proteins (Jones and Safinya 2008) also supports the hypothesis that the L-tails form a solvated polymer layer around the core. It seems reasonable to assume that, due to an excess negative charge on the NF core and a significant amount of glutamic acid residues in the NF-L projection, they are expelled from and repelled by the backbone, especially at low ionic strengths. The role of α-internexin is even less certain. This protein has a relatively short projection, $N_\alpha = 92$ (Human Intermediate Database, http://www.interfil.org), which is also much less charged than the NF-L tail.

In our previous publications (Zhulina and Leermakers 2007a, b, 2010; Leermakers and Zhulina 2008), the self-consistent field (SCF) technique was used to study the physical chemical features of the NF corona comprising L-, M-, and H-projections. The projections were described with amino acid resolution. That is, the primary aa sequences in all projections are taken as an input. Next, the aa residues are grouped according to charge and

hydrophilic/hydrophobic properties, giving rise to five types of segments with different interaction parameters. The cylindrical brush of coarse-grained projections is put in an aqueous solution at fixed ionic strength and pH. The electrostatic interactions are accounted for within the Poisson–Boltzmann framework, whereas the chain statistics obey the freely jointed chain (FJC) model. A two-gradient (2D) version of the SF-SCF model allows for the density distribution profiles of the system components in the two directions, i.e., parallel and perpendicular to the NF core. In a computationally more efficient one-gradient (1D) SF-SCF model, the density distributions are averaged over lateral and angular coordinates, and therefore depend only on distance from the NF core. This model was used in our previous studies (Zhulina and Leermakers 2007a, b) to monitor coronal transformations triggered by variations in ionic strength, pH, and levels of the degree of phosphorylation of the projections. We demonstrated that variations in pH close to the physiological value (~ 7) have no noticeable effect on the structure of the NF corona. A dramatic coronal shrinkage is, however, anticipated at pH $\sim 4-5$ due to suppression of the degree of ionization of acidic residues (Zhulina and Leermakers 2007b). At low solution salinities, the NF brush is highly swollen due to electrostatic repulsion between the tails. In a dephosphorylated state the longest H-projections reside close to the NF core, embedded in a sublayer of the shortest L-projections. The intermediate M-tails are expelled to the periphery of the corona, while being forced into a flower conformation (Zhulina and Leermakers 2007a). Enzymatic phosphorylation of the KSP motifs in the H- and M-tails triggers a major relocation of the H-projection. These change their conformation from being mainly near the core to be in a flower state with the crown at the periphery of the corona. As a result, the NF brush becomes thicker. An increase in NF thickness was experimentally demonstrated in an in vitro study on reconstituted filaments (Kumar and Hoh 2004). The propensity of the H-tails to cross-bridge (Chen et al. 2000) might also increase when KSP motifs are phosphorylated. The latter is essential in the formation of a NF network, envisioned as a parallel array of inter-acting neurofilaments (Leermakers and Zhulina 2008). An increase in the ionic strength leads to a decrease in the coronal thickness, and makes the differences in the projection density distributions less dramatic. Nevertheless, in the current parameter setting, phosphorylation-induced translocation of the H-tails is seen up to the physiological ionic strength of ~ 0.15 M (Zhulina and Leermakers 2007b).

To highlight the roles of different projections in the NF corona, we varied the molar ratio of the M- and H-tails (Zhulina and Leermakers 2010). Variations in the coronal composition indicated a mediating role of the shortest L-projections. According to the SF-SCF model, L-tails form a distinct sublayer near the filament core that might absorb or expel the H-tails in a phosphorylation-dependent manner.

The goal of this work is to examine physical chemical features of the L-projections using the one-gradient (1D) SF-SCF machinery. In this study we show that the L-chains, which are mainly negatively charged poly-ampholytes, form a subbrush (Fig. 1) with an approximately parabolic electrostatic potential. The electric field associated with the L subbrush can expel a larger macro-molecule (e.g., H- or M-projection) in an ionization-dependent manner. To obtain greater insight into the properties of this L subbrush, we varied its composition by exchanging the L-tails with the less charged projections of α-internexin, and analyzed how such substitution affects the phosphorylation-triggered translocation of the H-tail. We show that progressive substitution of L-tails by shorter projections of α-internexin decreases the electrostatic potential in the L subbrush and shifts the translocation of H-tails to higher levels of phosphorylation.

The remainder of the paper is organized as follows. In "SCF theory and the molecular model" we briefly review the basics of the SF-SCF numerical method and formulate the molecular model of NF projection domains. In "Results and discussion" we present the results of the SCF calculations and compare these with relevant experimental data. In "Conclusions" we summarize our findings.

SCF theory and the molecular model

We start with a brief review of the key ingredients of the SCF theory. A more detailed discussion of this method can be found elsewhere (Fleer et al. 1993). For each segment type X (segments are mentioned below) in the system, there are two complementary distributions, namely the volume fraction φ and the potential u profiles. $\varphi_X(r)$ is the dimensionless concentration of segment X at coordinate r, and $u_X(r)$ is the potential felt by segment X at coordinate r. A mean-field free energy F is a functional of these distributions. The optimization of this free-energy functional leads to the self-consistent field algorithm which can formally be expressed as

$$\varphi[u(r)] \leftrightarrow u[\varphi(r)]. \tag{1}$$

In words, the left-hand side of this equation says that the volume fractions (of any type) can be computed from the segment potentials (of any type), and the right-hand side specifies that the potentials can be evaluated from the volume fractions. When the volume fractions and segment potentials on the left- and right-hand sides are identical, the system is referred to as being self-consistent (SC) and the

fixed point is known as the self-consistent field (SCF) solution.

To obtain the volume fractions from the potentials we use a freely jointed chain (FJC) approximation. Especially for a dense array of end-grafted polymers, in which the chains are strongly stretched, the FJC model produces reliable results also because entanglements and chain backfoldings are rare. The segment potentials consist of three volume-fraction-dependent terms: (1) There is a contribution proportional to the volume of the segments that specifies the insertion energy. This contribution is linked to the incompressibility constraint. (2) The short-range interactions are accounted for in a Bragg–Williams approximation, and well-known Flory–Huggins interaction parameters specify the effective interaction energy for unlike contacts. (3) For charged segments there is an electrostatic contribution. Similarly to in Poisson–Boltzmann theory, the potentials follow from solving the Poisson equation. pK_a and pK_b values are assigned to acidic and basic amino acids, and the degree of dissociation is evaluated locally in the brush, accounting for both the pH and the local electrostatic potential.

Accurate SCF solutions of Eq. 1 are routinely generated numerically. For this, a discretization scheme is necessary. Here we follow the procedure of Scheutjens and Fleer, who suggested use of the segment length a to discretize space. In this method the segments can only sit on a discrete set of coordinates, and the volume of the lattice sites is set to a^3. The lattice sites are arranged in a cylindrical geometry, and along the radial direction and parallel to the long axis of the

cylinder mean-field averaging is implemented. Only gradients in volume fractions in the normal direction (r) are accounted for.

Besides "polymeric" projection domains (specified below) we have three types of monomeric species (all with linear size a), representing water (W), a monovalent cation (Na), and corresponding anion (Cl). Also for the monomeric species there is a segment potential with the three above-mentioned contributions. The volume fractions of the monomeric species follow from Boltzmann's law, and the normalization is chosen such that the distributions approach the bulk values far outside the brush (grand canonical ensemble).

The primary amino acid sequence is the starting point of the modeling of the projection domains. Each aa residue is seen as an isotropic monomer with size $a = 0.6$ nm. A simplification is carried out by grouping the aa into five "segments" (**C**, **M**, **P**, **N**, **A**; see Table 1). The **C**-segment is the serine that is found in KSP motives. Segment **M** represents the acidic (negatively charged) amino acids. The positively charged amino acids are referred to as **P**. All neutral and reasonably soluble amino acids are collected in **N**, and finally there are the apolar amino acids **A**. The coarse-grained sequences of H-, M-, and L-tails and of α-internexin projection are presented in Table 1. The values of various interaction parameters used for each of the segments (**C**, **M**, **P**, **N**, **A**) are presented in Table 2. Around physiological conditions we assume that nonelectrostatic interactions compete with the electrostatic ones, and reasonably accurate values for the nonelectrostatic parameters

Table 1 Coarse-grained projection domains

NF-H chain

NA$_4$N$_2$A$_2$ MA$_3$PA$_2$ NAN$_3$(AP)$_2$N M$_2$(PA)$_2$AM PNMP MNA$_3$(M$_2$N$_2$)$_2$ (ANM$_2$)$_2$M$_2$PM (APM$_3$)$_2$A$_2$M$_4$A MA$_2$M$_3$N PCA$_3$M$_2$ A$_2$NAM PMAP CA$_2$PM$_2$ APCA$_2$ MAPC AMPM$_2$ APCA$_2$ MAPC AMPA PCA$_2$P M$_2$APC A$_2$MAP CAMP M$_2$APC A$_2$MAP CAMP APCA$_2$ PM$_2$AP CA$_2$MA PCAM PAPC A$_2$PM$_2$A PCA$_2$M APCA$_2$ PM$_2$AP CA$_2$ MA PCAM PAPC ANPM$_2$ APCA MPAP CAMP M$_2$APC AMPA PCA$_2$P AMAP CAMP APCA$_2$ PAMA PCAM PAPC A$_2$PM$_2$A PCAM PAPC A$_2$PM$_2$A PCAM PAPC A$_2$PM$_2$A PNAM PAPC A$_2$PM$_2$A P(CAMPAP)$_2$NA MAPC AMAP NA$_2$PM$_2$ APNA$_2$ MPNA MPA PCA$_2$P M$_2$APC AMPA PCA$_2$P M$_2$APA$_2$ MPMA$_2$ P$_2$M$_2$AP CA$_2$PM$_3$PA-NM(AP)$_2$MA$_2$ P$_2$AM$_3$P A$_3$NAP NM$_2$P$_2$M NP$_2$M$_2$A$_2$ P$_2$MA$_2$(PA)$_2$ M$_2$P$_2$MA$_3$ MPAP MNPA MAP$_2$M$_2$ AM$_2$P$_3$A$_2$ NAMP MA$_3$PA MAPM$_2$ (AP)$_2$MPN MA$_2$P$_2$M AM$_2$(AP)$_2$M ANPA$_2$M P$_2$MA$_3$M P$_2$MNP M$_2$PAP$_2$ AM$_2$PA PNM(AP)$_2$ M$_3$PNA NPMA N(PA)$_2$MP AMPN$_4$(MNP)$_2$ A$_2$MPA NM$_2$PA (AP)$_2$

NF-M chain

N$_3$A$_2$(NA)$_2$A$_2$ N$_3$PA$_3$N AN$_2$PA NPNP AMA$_2$ (PA)$_2$ N$_2$PNA M$_2$A$_2$M$_2$N PAM$_3$P NMAM$_2$ (A$_2$N)$_2$M$_2$A$_3$N APM$_2$P$_2$ MA$_2$M$_2$P M$_3$(AM)$_2$M$_3$A$_3$ P$_2$CA$_2$P ANA$_2$MA PM$_3$AM PM$_4$AN M8A$_2$P NMNA M$_2$A$_2$NM PMAN$_2$ MPM$_2$A MNM$_2$A MNM(AM)$_3$(MA)$_2$PM$_2$P$_2$ AM$_2$PN M$_2$A$_2$NP M$_2$A$_3$MA PAMP AMPA PCA$_3$P CA$_2$M$_2$P APCA$_3$ PCA$_2$M$_2$ PAPC A$_3$PCA$_2$ M$_2$PAP CA$_3$PC A$_2$M$_2$PA PCA$_2$NPCA$_2$M$_2$ PAPC A$_3$PCA$_2$ M$_2$APN PAMA$_2$ PAMN PM$_3$PM APMA$_2$ PM$_2$PA MP$_2$M$_2$P APMA$_2$ MP$_3$AM NA$_2$PM$_2$ A$_3$MA$_2$N ANPN APAN AMPM NPM$_2$A PA$_2$N$_2$(MP)$_3$ A$_3$MA$_2$N M$_3$ANM PA$_2$PA NP$_2$M$_2$A$_3$ N(AM)$_2$AP M$_2$A(MN)$_2$P MPAN APM$_3$P A$_3$N$_2$A$_2$M ANA$_2$M$_2$P$_2$A$_2$MP NM$_2$PA$_3$ NPNA MPAN$_2$ (MA$_2$)$_2$(NPNA)$_2$NA N$_2$PA(M$_2$N)$_2$ NM$_2$PA$_2$ N$_2$P$_2$A$_2$M PAN$_3$A$_3$ PMAN$_3$M

NF-L chain

N$_3$A$_2$(NAN)$_2$N$_4$ (NA)$_2$P(NA)$_2$A$_2$ N$_5$A$_2$N$_2$P N$_2$AN$_6$A NM$_2$N$_2$M AM$_2$NA MANP AM$_2$AP M$_2$A$_2$N(MA)$_2$ M$_4$(PM)$_2$M(AM$_4$A)$_2$M$_4$A PM$_2$NM$_2$ APM$_4$A$_2$ M(AM$_2$)$_2$NP MAM$_4$P$_2$ AMA$_3$M$_2$ NA$_2$P$_3$M

α-Internexin:

N$_3$A$_2$NA NA$_2$NA$_3$ NAN$_2$A$_4$PA$_2$NA N$_3$PAN$_3$ A$_2$NAP$_2$ M$_6$ANP A$_2$NP$_2$N$_3$ A$_2$MN$_2$M$_2$ A$_2$M$_2$NA$_2$ N$_2$P$_2$NM PN$_2$AM$_2$ N$_2$AN$_3$PA

A subscript number after a segment name (or sequence) indicates the length of a repeat. The following amino-acid assignments were made: $\mathbf{A} \in \{G, P, C, M, A, L, V, I\}$, $\mathbf{N} \in \{Y, Q, H, F, W, T, S'\}$, $\mathbf{P} \in \{K, R\}$, $\mathbf{M} \in \{E, D\}$, $\mathbf{C} \in \{S\}_{KSP}$

Table 2 List of all Flory–Huggins interaction parameters χ and the valency v; for some segments more values are given, representing either the limiting values for low or high pH (P, N) or the level of phosphorylation (C)

χ	Na	Cl	A	N	P	M	C	W	S	v	ε
Na	0	0	2	0	0	0	0	0	0	1	5
Cl	0	0	2	0	0	0	0	0	0	−1	5
A	2	2	0	1	1	1	1	2	0	0	2
N	0	0	1	0	0	0	0	0.6	0	0	5
P	0	0	1	0	0	0	0	0	0	0, 1	5
M	0	0	1	0	0	0	0	0	0	0, −1	5
C	0	0	1	0	0	0	0	0.6	0	0, −1, −2	5
W	0	0	2	0.6	0	0	0.6	0	0	0, 1, −1	80
S	0	0	0	0	0	0	0	0	0	−0.025	2

The last column gives the relative dielectric constant ε

become important. We note, however, that the parameter set has not reached the status of "established" yet, even though the present levels of coarse graining do not permit its refinement. As a result, we feel that the trends predicted by the theory are more of interest than representing absolute values.

Both NF-M and NF-H projections have a number of KSP repeats that are subject to enzymatic phosphorylation. In principle the phosphorylation is a discrete effect. In the model, however, this is implemented by assigning a (partial) valence $-2 \leq v_C \leq 0$ to the serines present in the KSP repeats. That is, the phosphorylation-induced charge $e\Delta Q_i$ on the tail of type i (i = H, M) is smeared out over all the serines in KSP motifs within the tail, and the valence is set to $v_C = \Delta Q_i/n_i$, where n_i is the total number of KSP repeats in tail i. Hence, $v_C = 0$ represents the dephosphorylated state. When half of the KSP repeats in the H- and M-tail are phosphorylated, $e\Delta Q_i = (-2e)n_i/2, v_C = -1$, and full loading gives $v_C = -2$. All other serines and threonines are assumed to be unaffected by the phosphorylation.

The projections are grafted onto a cylinder (surface S) with radius $R = 8a$ that mimics the NF core. For all NF brushes considered in this paper, exactly 12 projections are tethered per core segment with length $l = 25a = 15$ nm. This grafting density corresponds to 32 projections per length of coiled-coil domain $l_c = 40$ nm. In a wild-type W-NF with molar ratio L:M:H = 7:3:2, one therefore finds seven L-, three M-, and two H-tails, and distances $d_L = l/7$, $d_M = l/3$, and $d_H = l/2$ between projections L, M, and H, respectively, along the backbone. Here, the distance d_i specifies the dimensionless coverage $\Theta_i = N_i a/d_i$ (where N_i is the number of monomers in the projection of type i = L, M, H), which amounts to $\Theta_L^W = 39.76, \Theta_M^W = 60.48$, and $\Theta_H^W = 48.56$ in a wild-type, W-NF. In some of the calculations we exchanged NF-L chains for α-internexin. In these calculations the total number of projections
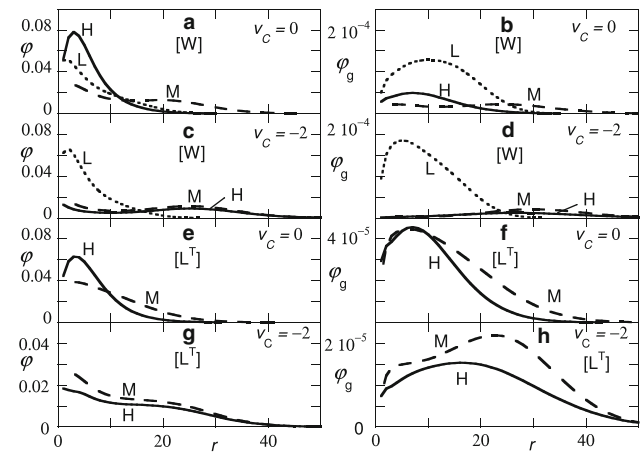

Fig. 2 **a**, **c**, **e**, **g** Radial volume fraction profiles $\varphi(r)$ of the L- (*dotted*), M- (*dashed*), and H-chains (*solid*), and (**b**, **d**, **f**, **h**) the corresponding free end distributions $\varphi_g(r)$ of isolated (*individual*) NFs under physiological conditions pH 7, $c_s = 0.15$ M. **a**, **b** Wild-type $v_C = 0$, **c**, **d** Wild-type $v_C = -2$. **e**, **f** Truncated L-chains (M and H only) $v_C = 0$. **g**, **h** Truncated L-chains $v_C = -2$

per unit length was fixed, $\Theta_M = \Theta_M^W = 60.48, \Theta_H = \Theta_H^W = 48.56$, while Θ_L ancan formally be expressed asd Θ_α were varied.

Results and discussion

We start with the systems that do not have the α-internexin projection incorporated. In the following the aim is to prove that the NF-L chains play an important role in maintaining the structure of the NF brush.

Polymer density profiles

In Fig. 2 we present radial volume fraction φr and corresponding end-point profiles $\varphi_g(r)$ of L, M, and H projections for wild-type (indicated by [W]) NFs at physiological conditions (pH 7, $c_s = 0.15$ M), at both low and high levels of phosphorylation of the KSP motifs and compare these with corresponding profiles for a NF-brush from which the L-chains have been removed, indicated by [L^T].

Referring to Fig. 2 we first mention a few characteristics of the wild-type brush, even though these have been discussed in our previous works already. It can be seen that the M-chain in wild-type NF is in the flower conformation (Skvortsov et al. 1997; Skvortsov et al. 2002) at both low and high degrees of phosphorylation. More specifically, the M-chain is subdivided into two domains: one, which is the "stem" of the flower, which is almost uniformly stretched and found close to the NF core, and another, which is referred to as the "head" or the "crown" of the flower, which is found at the periphery of the NF brush. The stem

length is approximately equal to the thickness of the L sublayer, and it contains a relatively small fraction of the aa residues. The head accounts for the majority of the aa residues, predominantly those from the distal part of the tail. This is seen by the distinct maximum in both the overall profile of the M-chains (Fig. 2a) and in that of the end-points (Fig. 2b). The M-flowers are better seen for high degree of phosphorylation and low ionic strengths (not shown). The conformations of the H-chain depend strongly on the degree of phosphorylation. As is clear from the end-point distribution (Fig. 2b) as well as the high density near the core (Fig. 2a), the H-chain is embedded in the L-rich region at low levels of phosphorylation and is in the flower conformation at high levels of phosphorylation. Phosphorylation-induced translocation of the H-chain will be used below to measure the influence of α-internexin.

The conformations of the head (crown) of the flower might provide clues to possible cross-bridging mechanisms by the long tails. Recent MC simulations of wild-type NFs, performed at low ionic strengths, indicated backwards bending of the terminal KEP domain of the H-tail (Chang et al. 2009). The hypothesis that H-tails might form loops and bridges due to the electrostatic interactions between KEP and KSP domains was discussed previously in the literature (Gou et al. 1998). To check whether the H-tail has this tendency under close to physiological conditions, we performed SF-SCF calculations of the wild-type NF brush, wherein peripheral parts of fully phosphorylated H-tails ($\nu_C = -2$) were modified by additional monomers ("markers"). These were inserted into the H-tail at regular intervals (one marker per SF-SCF calculation). The marker with ranking number $s = 0$ is located at the boundary between the KSP and KEP domains (between aa residues 191 and 192 from the tail free end), $s > 0$ and $s < 0$ indicate positions of the marker within the KEP and KSP domains, respectively. The most probable position $\langle z_s \rangle$ of a marker at ranking number s was evaluated by the SF-SCF calculations and plotted as a function of s. Figure 3 shows the most probable position $\langle z_s \rangle$ as a function of the ranking number s at three ionic strengths, $c_s = 0.001$, 0.01, and 0.1 M. In all three cases, $\langle z_s \rangle$ passes through a broad maximum at $s_{max} \approx -50$. This proves that the "trajectory" (the most probable path) of the KEP domain is bent backwards. A negative value of s_{max} indicates that the KEP and KSP domains "overlap." That is, the KEP domain and part of the KSP domain are found in the same cylindrical sublayer of the NF brush. Although the difference in $\langle z_s \rangle$ for starting ($s = 0$) and terminal ($s = 191$) residues of the KEP domain is modest (about $7a$, $5a$, and $3a$ for $c_s = 0.001$, 0.01, and 0.1 M, respectively), a loop-like configuration of the KEP domain and its overlap with the KSP domain are detected in the SF-SCF model up to physiological conditions.
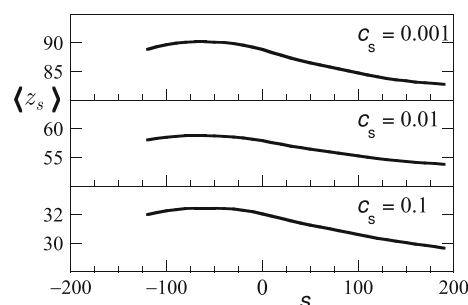

Fig. 3 The most probable position $\langle z_s \rangle$ of a marker with ranking number s as a function of the position of the marker as indicated by the ranking number s, for three values of the ionic strength as indicated. Here the ranking number $s = 0$ is at the end of the KSP domain, i.e., between the end of the KSP and the beginning of the KEP domain

The truncation of L-chains from the wild-type NF corona has major consequences for the brush structure. Both the end-point distributions (Fig. 2f,h) as well as the overall density distributions (Fig. 2e,g) indicate that, in the absence of L-chains, the M- and H-chains do not develop flower conformations. The density profiles resemble those found for a "conventional" cylindrical polyelectrolyte brush (Qu et al. 2009). The NF brush with truncated L-tails extends with increasing degree of phosphorylation as expected. This does not exclude, however, the possibility that H-tails bend backwards. Our recent 2D SF-SCF calculations demonstrated that loop conformations are found even in an isolated phosphorylated H-tail tethered to a negatively charged or neutral surface (not shown).

In a related paper (Zhulina and Leermakers 2010) we considered the effects of removing M- and/or H-projections from the wild-type NF. Also the exchange of M-chains with H-chains and vice versa was studied. In all of these scenarios only modest changes were observed, definitely less dramatic than on deleting L-chains. This clearly points to the role of the L-projections in providing a reservoir for the H-chains at low levels of phosphorylation, and as a medium that enforces the flower conformation at high degrees of phosphorylation. For this reason we now assign the proximal region of the corona rich in L-chains as the subbrush region and refer to the remainder of the corona as the outer corona.

Brush thickness

To quantitatively characterize the thickness of the L subbrush, we adopt a procedure described earlier (Zhulina and Leermakers 2010). In short, we place a filament in an impermeable cylindrical tube of radius $R + D$ with the core oriented along the tube axis. The mirror boundary condition imposed at the edge of the tube $r = R + D$ mimics the presence of neighboring filaments. By

compressing this NF (by decreasing the tube size D) we calculate the interaction free energy F^{int} per unit length of the filament. Figure 4 gives the dependence $F^{int}(D)$ for a pure L-filament, i.e., a filament composed solely of NF-L molecules ($\Theta_H = \Theta_M = 0, \Theta_L = 68.16$, denoted as [L]), and for a NF with truncated long M- and H-tails ($\Theta_H = \Theta_M = 0, \Theta_L = 39.76$, denoted as [$M^T H^T$]). The latter corresponds to a lower grafting density of the L-tails. Here, the free energy is expressed in units of $k_B T$, and D is measured in units of monomer size $a = 0.6$ nm. As indicated by Fig. 4, the interaction free energy $F^{int}(D)$ is purely repulsive in both cases. We evaluate the "mechanical" brush thicknesses D_1 and D_2 from the respective conditions $F^{int}(D_1) = 0.002 k_B T$ and $F^{int}(D_2) = 0.01\ k_B T$. The former condition corresponds to a repulsion of $\sim 1 k_B T$ per persistence length of a NF and, therefore, to the "onset" of NF–NF alignment. The latter condition corresponds to a repulsion of $\sim 10 k_B T$ per persistence length, which is sufficient to prevent any further approach of neighboring NFs. For pure L-filaments and for $M^T H^T$-NFs, we find $D_1 \approx 27a \approx 16$ nm, $D_2 = 25a = 15$ nm, and $D_1 \approx 24a \approx 14$ nm, $D_2 = 22a \approx 13$ nm, respectively. Clearly, a decrease in coverage of the L-tails from $\Theta_L = 68.16$ in a pure L-filament to $\Theta_L = 39.76$ in $M^T H^T$-NF leads to some decrease in the brush thickness. However, in both cases, the L-chains are still stretched with respect to their Gaussian size ($a\sqrt{N_L} \approx 12a$), which justifies the application of brush concepts to the L-projections.

A recent in vitro study on reconstituted NFs with varied H:M:L ratios (Jones and Safinya 2008) revealed a number of relevant observations. The small-angle X-ray scattering (SAXS) in solutions of reconstituted NFs demonstrated that, under close to physiological conditions, the NF–NF spacing changed with protein volume fraction Φ as $\Phi^{-1/2}$, indicating nematic-type ordering of the NFs at relatively high values of Φ. As a result, the longitudinal orientation of NFs in such solutions permits direct comparison between the experiments and our SF-SCF model. According to Jones and Safinya (2008), the closest interfilament spacing

between pure L-filaments detected from the scattering data was 38 nm. Using the 28 nm spacing between filament cores (each of radius $R = 5$ nm), the authors estimated the thickness D of the L-brush as 14 nm.

In a subsequent study (Beck et al. 2010), liquid-crystalline hydrogels of reconstituted NFs were subjected to an osmotic pressure, which mediated the average NF–NF distance. The pressure–distance curves were measured for pure L-filaments and NFs with varied M-to-H ratio. Comparison between the data for L-filaments (Beck et al. 2010) and the theoretical force–distance dependence, obtained by numerical differentiation of the interaction free energy $F^{int}(D)$ of Fig. 4, demonstrates that: (1) the measured and calculated forces between L-filaments are purely repulsive, (2) the shapes of the theoretical and experimental curves are similar, and (3) the experimental value of force systematically exceeds the corresponding theoretical value by about an order of magnitude. The latter might be attributed to weaker ordering of L-filaments in NF gels compared with the parallel NF orientation assumed in the theoretical model.

The morphological analysis of axoplasms in model animals—transgenic mice with selectively modified NF projections (Rao et al. 2002; Garcia et al. 2003)—indicated that, in mice that lacked both H- and M-tails, the median spacing between neurofilaments was reduced to 30 nm compared with 45 nm in control (wild-type) animals. Assuming that L-projections in such in vivo filaments can be envisioned as a $M^T H^T$ corona, and modeling the axonal NF network as a parallel array of interacting NFs, the SF-SCF theory estimates the median NF–NF distance as 31 nm (Zhulina and Leermakers 2010). For a pure L-filament, the median distance would increase to 34 nm. Clearly, the correspondence between the theoretical predictions and the available experimental data is quite reasonable.

Electrostatic potential

To obtain deeper insight into the role of L-projections, we considered the electrostatic field created in the L subbrush. Figure 5a presents the electrostatic potential ψ (in Volts) for a pure L-filament as a function of the square of the distance r (i.e., r^2) from the NF core at three different ionic strengths, $c_s = 0.15$, 0.01, and 0.001 M. The linear portions of the plots indicate a parabolic $\psi(r)$ dependence. The parabolic shape of the electrostatic potential is perturbed in the vicinity of the NF core, i.e., at $r = 0$ (the sharp dip is due to the surface charge of the core; see Table 2) and at the edge of the brush (where the terminal segments of tethered chains become unstretched). Indeed, in the intermediate range of r values the parabolic formula, $\psi(r) = A + Br^2$, where the intercept A depends on the
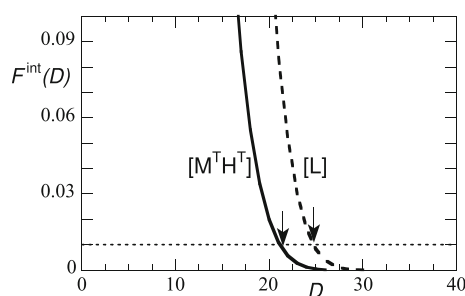

Fig. 4 Free energy $F^{int}(D)$ in units of $k_B T$ with D in units of a for [$H^T M^T$]-NF (*solid line*) and pure L-filament (*dashed line*) at physiological conditions. The *arrows* indicate values of D_2 (corresponding to $F^{int} = 0.01 k_B T$). $D_2 \approx 25$ and $D_2 \approx 22$ for [$M^T H^T$] and L-filament, respectively

ionic strength c_s, and the slope B is independent of it (indicated by solid lines in Fig. 5a), turns out to be a good approximation for the electrostatic potential in the L-brush. Such behavior of the electrostatic potential ψ was predicted theoretically for planar brushes of monodisperse flexible polyelectrolytes (Zhulina et al. 2000). The potential profile ψ is parabolic when the tethered polyelectrolytes are noticeably stretched with respect to their Gaussian size and the nonelectrostatic interactions between monomers are weak compared with the electrostatic repulsions. In a cylindrical geometry, the parabolic shape of ψ could be considered as an approximation only. However, the data in Fig. 5a proves that the electrostatic potential in the L-brush is reasonably well approximated by a parabola. Note that, although the extension of a parabolic part of the potential $\psi(r)$ decreases upon an increase of the ionic strength c_s, the latter is still traced up to physiological conditions, i.e., $c_s = 0.15$ M.

The presence of long projections does not significantly affect the electric field within the L-brush. Figure 5b demonstrates this. In this graph the electrostatic potential
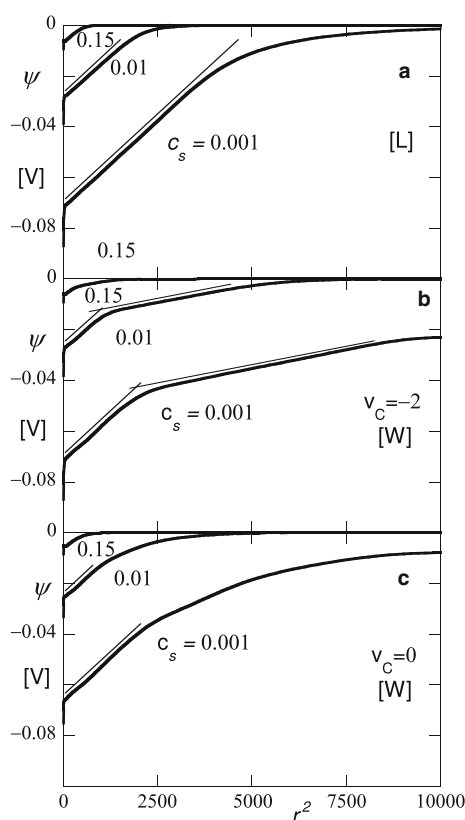

Fig. 5 Electrostatic potential ψ (in Volts) as a function of the square of the distance r^2 from the core surface, **a** for pure L-filaments, **b** for wild-type W-NFs, $v_C = -2$, and **c** for W-NFs, $v_C = 0$, at different salt concentrations as indicated. The *straight portions* of the plots indicate a parabolic shape of ψ. Three values for the ionic strength are used: 0.15, 0.01, and 0.001 M. The *thin lines* along the *curves* facilitate the identification of the *parabolic regions*

$\psi(r)$ for a wild-type W-NF is given for the condition that the KSP motifs are strongly phosphorylated ($v_C = -2$), while the ionic strength is the same as in Fig. 5a. Clearly, the presence of polyelectrolytic M- and H-tails leads to a larger range of $\psi(r)$. In addition, the ψ versus r^2 dependence now has two linear parts: the first one (at small r) is due to the L-brush, and the second one is attributed to the expelled M- and H-tails. When, however, the electrostatic tail−tail interactions in the second layer are weak (e.g., H- and M- tails are dephosphorylated; Fig. 5c), the shape of the electrostatic potential $\psi(r)$ noticeably deviates from a parabola in the outer corona. A similar behavior of ψ is expected for NFs with selectively truncated long tails.

Effect of α-internexin

Results of the SF-SCF model of the NF brush suggest that the L-tails might regulate the conformations of the longer M- and H-tails. This regulation is mediated by phosphorylation of KSP motifs present in both M- and H-tails. Recently, the protein α-internexin has been identified as a fourth NF component in small-caliber axons (Yuan et al. 2006). The concentration of α-internexin varies at different stages of central nervous system development, and it is comparable to that of NF-L in small axons of adult brain (Stettler et al. 2006). In optic axons of mice, the molar ratio of α-internexin and NF-L is close to 1:2 (Yuan et al. 2006). Human α-internexin has an unstructured projection domain that is $N_\alpha = 92$ aa residues long and has only $\Delta Q_\alpha \approx 3$ excess negative charges (Human Intermediate Filament Database, http://www.interfil.org). As a result, the projection domain of α-internexin (abbreviated here as the α-projection) is weakly charged compared with the L-tail. To a first approximation, the addition of α-projection into the NF brush with a ratio α-internexin:NF-L = 1:2 can be envisioned as a substitution of one-third of all the L-tails by α-projections at fixed amounts of M- and H-chains. In such an NF, the chain population is given by Θ_i ($i = H, M, L,$ and α) with values $\Theta_H = \Theta_H^W = 48.56$, $\Theta_M = \Theta_M^W = 60.48$, $\Theta_L = 2\Theta_L^W/3 = 26.51$, and $\Theta_\alpha = \Theta_L^W N_\alpha/3N_L = 8.59$.

In Fig. 6 we compare the density profiles of the various projections $\varphi_i(r)$ ($i = H, M,$ and L) in a wild-type corona (Fig. 6a, b), a corona with an experimentally relevant ratio of α-internexin:NF-L = 1:2 (Fig. 6c,d) with a neurofilament wherein all L-chains are replaced by α-internexin. In these graphs we give results for both the dephosphorylated ($v_C = 0$) and the fully phosphorylated ($v_C = -2$) states of the KSP motifs. In all cases the α-projections are confined near the NF core. The exchange of L-chains with α-internexin has minor effect on the density distributions of the M- and H-tails. This is true for relatively modest variations in the ratio L:α. However, large amounts of α-internexin (close to full substitution of L-chains) lead to

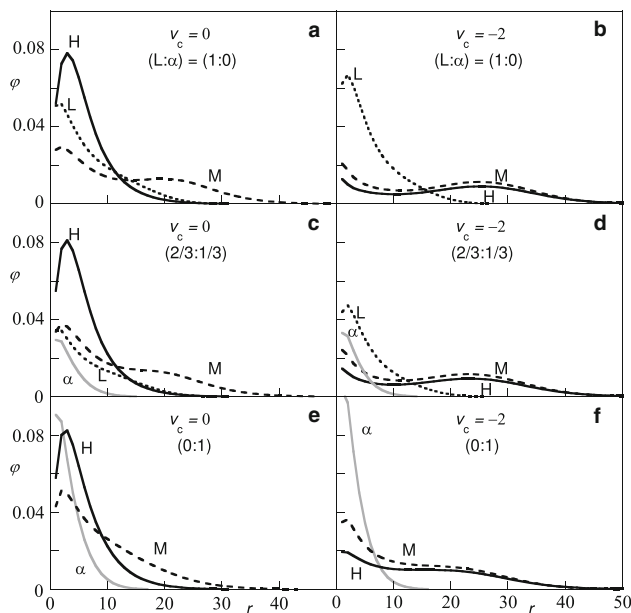**Fig. 6** Radial volume fraction distributions **a**, **b** for a NF with H-, L-, and M-chains as indicated. **c**, **d** For a NF with part of the L-chains substituted by α-internexin; mixing ratio: 2/3 L- and 1/3 α-internexin chains. **e**, **f** for a NF with all L-chains replaced by α-internexin. In **a**, **c**, **e** the M- and H-chains are not phosphorylated, $v_C = 0$, while in **b**, **d**, **f** the chains are fully phosphorylated, $v_C = -2$. pH is 7, and ionic strength is near physiological $c_s = 0.15$ M

lines). Variations in the electrostatic potential ψ that might be attributed to the presence of α-internexin (admittedly small under physiological conditions) may serve as a fine-tuning mechanism in, e.g., possible association of cyto-skeletal and/or other proteins with NFs.

In Fig. 8 we have collected the average heights of the H-tail (computed from the first moment of the end-point distribution) as a function of the level of phosphorylation of the KSP motifs for: (a) W-NF (the reference), (b) Wα-NF with a 2:1 ratio of L to α-internexin, and (c) NFs for which all L-tails are substituted by α-projections. As seen from Fig. 8, the translocation of H-tail [sudden change in $h_H(v_C)$] is only slightly shifted to larger values of $|v_C|$ when one-third of the L-tails are substituted by α-projections (Fig. 8b). The relocation transition is, however, strongly modified when all the L-tails are substituted by α-projections (Fig. 8c). In the latter case, the phosphorylation-induced translocation of H-tail becomes significantly less cooperative, and expelled M- and H-tails lose the flower conformation.

From a physical perspective, dilution of L-tails by adding weakly charged α-projections decreases the electric field in the subbrush of L- and α-projections (Fig. 7). The latter are localized near the NF core and mostly enhance the nonelectrostatic interactions. The L subbrush is less stretched, and the phosphorylation-induced expulsion of the H-tail is shifted to larger values of $|v_C|$. This effect is noticeable at relatively large α-to-L ratios. Therefore according to the SF-SCF model, the properties of a neurofilament (NF brush thickness, frequency of cross-bridges, etc.) might be tuned by the inclusions of α-internexin.

As discussed by Yuan et al. (2006), greater proportions of α-internexin in neurofilament might confer greater plasticity of NF network by modifying the cross-linking capabilities of NF populations. This hypothesis is consistent with the SF-SCF modeling of NF network. We have demonstrated in our previous study (Leermakers and Zhulina 2008) that, in the scenario that M-tails do not make cross-bridges, phosphorylation of KSP motifs enhances cross-bridging between H-tails. When M-chains also make cross-bridges, the effect holds at moderate levels of

noticeable changes in the coronal structure. Inspection of Fig. 6e, f clearly shows that the M- and H-chains have a less rich profile compared with the systems with sufficient amount of L-chains (Fig. 6a–d).

In Fig. 7 we demonstrate how the insertions of α-internexin change the electric field in the L-brush. Here, we fix the solution salinity, $c_s = 0.01$ M and $c_s = 0.15$ M in panels a and b, respectively, and plot the electrostatic potential $\psi(r)$ for L-filament with different ratios of α-projections to L-tails (indicated at the curves). Decreasing the ionic strength increases the absolute value of the electrostatic potential throughout the brush. Especially in the subbrush region there are significant differences for the electrostatic potential profiles between wild-type NFs (solid line) and α-internexin substituted ones (discontinuous
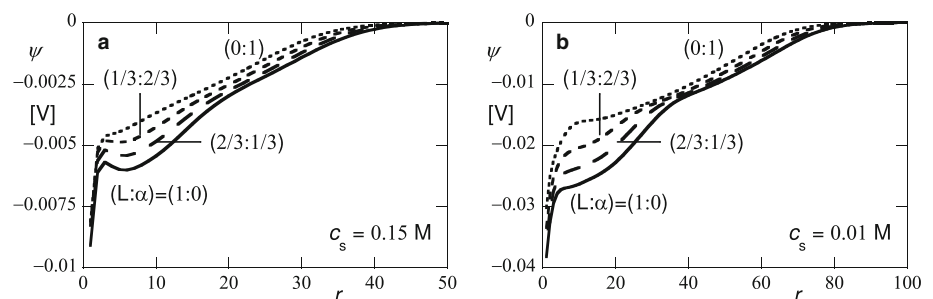

Fig. 7 The radial electrostatic potential $\psi(r)$ (in Volts) profile for various L to α-internexin ratios, as indicated. **a** $c_s = 0.15$ M and **b** $c_s = 0.01$ M. pH is 7
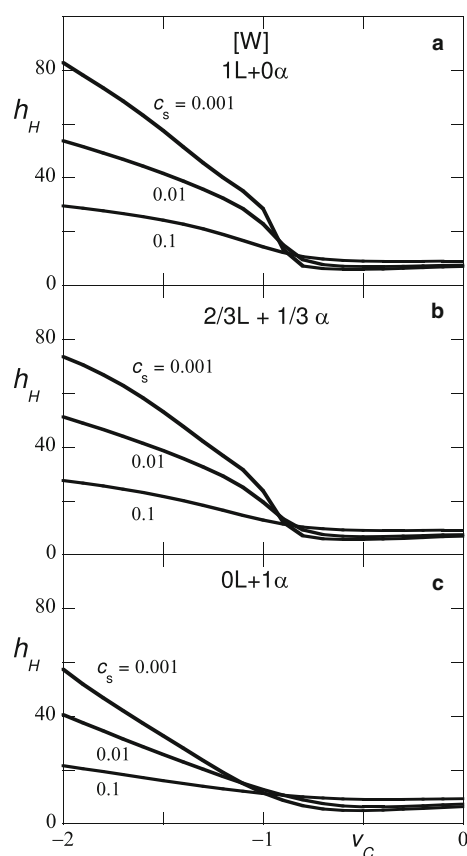
Fig. 8 The first moment of the end-point distribution of the H-chain, h_H as a function of the degree of phosphorylation as given by the valency of the serines in the KEP motifs, v_C. The function $h_H(v_C)$ can be used to evaluate the translocation transition of the H-tail in NF brushes with various L to α-internexin ratios: **a** 3:0 (wild type), **b** 2:1, and **c** 0:3 (all L-chains substituted by α-projections). Three values of the ionic strength c_s are used as indicated, and pH is 7; H- and M-chains are as in wild type

phosphorylation $|v_C| \lesssim 1$ (and is reversed at larger $|v_C| \lesssim 2$). That is, a moderate increase in $|v_C|$ leads to an increase in frequency of cross-bridges between H-tails in an NF network modeled as a parallel array of interacting NFs. According to the results of this study, insertion of considerable amounts of α-internexin projections in the NF brush, and the corresponding decrease in charge and expulsive potential of the L + α sublayer, diminish the number of available cross-linking domains of H-tails at the brush periphery. (The phosphorylation-induced translocation of H-tail is shifted to larger value of $|v_C|$.) Therefore, the frequency of cross-bridges between H-tails is expected to decrease upon an increase in the α-to-L ratio. Provided that extensive cross-linking makes the NF network less dynamic, an expected decrease in the tail cross-bridging due to insertions of α-internexin correlates with experimentally detected high dynamics of small axons in adult brain (Stettler et al. 2006).

When all L-tails are substituted by α-projections, the density profiles of M- and H-tails are similar to those in a wild-type NF with truncated L-tails (L^T filament). From a regulatory point of view, the removal of all L-chains is not a desirable situation.

At this stage, it should be realized that the SF-SCF framework has a number of inherent limitations. In addition to the mean-field approximation and the neglect of charge–charge correlation effects, our current model focuses only on the local structural features of NFs, e.g., the density profiles of various projections, conformational rearrangements triggered by variations in physical chemical conditions (pH, c_s, v_C, etc.), and the response to uniform NF compression. It does not account for the long-range correlations between NFs and other cytoskeletal elements mediated by specific protein–protein interactions. At the same time, the SF-SCF model is able to probe the response of local NF organization to variations in environmental conditions and to incorporate (under certain simplifying assumptions) cross-bridging NF–NF interactions. Rearrangements of projection domains in a NF brush might, in turn, be linked to possible roles (functions) of the neuronal proteins; for example, the insertions of α-internexin in neurofilament might possibly mediate the NF cross-bridging capacity.

Conclusions

In this paper we applied the one-gradient (1D) version of the SF-SCF model to explore the equilibrium structure of a neurofilament with given H:M:L tail ratio, which differed from wild-type composition. The projection domains of NF-L, NF-M, and NF-H proteins were coarse-grained to conserve the major features of the actual primary sequence of aa residues. We introduced five groups of segments (**A**, **N**, **P**, **M**, and **C**) that collect the aa residues with different charges and hydrophobicities, and imposed cylindrical symmetry on the NFs. This is justified by the large aspect ratio $l_p/D \gg 1$, where D is the diameter of these filaments.

Comparison of wild-type NFs with those with truncated L-tails allowed us to highlight the role of L-tails as a possible regulator of NF brush organization. In the framework of the SF-SCF model, L-tails are repelled from the NF core and create a polyelectrolyte subbrush that has, to a good approximation, a parabolic electrostatic potential profile. Although much shorter than the M- and the H-tails, the L-tails mediate the positioning of long tails in a cooperative fashion. More specifically, phosphorylation of the KSP motifs leads to rather abrupt relocation of the H-tails from the NF core to the outside of the NF brush. When the L-tails are removed, we noticed important changes in the conformations of the phosphorylated M- and

H-tails. The latter lose their flower conformation, and the NF brush thickness decreases.

Substitution of 33% of the L-tails by projections of α-internexin does not noticeably affect the behavior of the long tails. The dilution of L-tails by projections of α-internexin decreases the electric field inside the subbrush of shorter (L) chains and enhances the nonelectrostatic interactions. As a result, somewhat stronger levels of phosphorylation of KSP motifs are required to relocate the H-tail. When all L-tails are substituted by α-projections, the translocation of the H-tail becomes less cooperative. Therefore, the structural properties of a NF brush (thickness, compressibility, frequency of cross-bridges) might be additionally regulated by the presence/absence of α-internexin.

References

Bathe M, Rutledge GC, Grodzinsky AJ, Tidorz B (2005) A coarse-grained molecular model for glycosaminoglycans: application to chondroitin, chondroitin sulfate, and hyaluronic acid. Biophys J 88:3870–3887

Brown HG, Hoh JH (1997) Entropic exclusion of neurofilament side arms: a mechanism for maintaining interfilament spacing. Biochemistry 36:15035–15040

Beck R, Deek J, Jones JB, Safinya CR (2010) Gel expanded to gel condensed transition in neurofilament networks revealed by direct force measurements. Nat Mater 9:40–46

Chang R, Kwak Y, Gebremichael Y (2009) Structural properties of neurofilament sidearms: sequence-based modeling of neurofilament architecture. J Mol Biol 391:648–660

Chen J, Nakata T, Zhang Z, Hirokawa N (2000) The C-terminal tail domain of neurofilament protein-H (NF-H) forms the cross-bridges and regulates neurofilament bundle formation. J Cell Sci 113:3861–3869

Fleer GJ, Cohen Stuart MA, Scheutjens JMHM, Cosgrove T, Vincent B (1993) Polymers at interfaces. Chapman & Hill, London

Fuchs E, Cleveland DW (1998) A structural scaffolding of intermediate filaments in health and disease. Science 279:514–519

Garcia ML, Lobsiger CS, Shah SB, Deerinck TJ, Crum J, Young D, Ward CM, Crawford TO, Gotow T, Uchiyama Y, Ellisman MH, Calcutt NA, Cleveland D (2003) NF-M is an essential target for the myelin-directed "outside-in" signaling cascade that mediates radial axonal growth. J Cell Biol 163:1011–1020

Gou JP, Gotow T, Janmey PA, Leterrier JF (1998) Regulation of neurofilament interactions in vitro by natural and synthetic polypeptides sharing Lys-Ser-Pro sequences with the heavy neurofilament subunit NF-H: Neurofilament crossbridging by antiparallel sidearm overlapping. Med Biol Eng Comput 36:371–387

Herrmann H, Aebi U (2004) Intermediate filaments: molecular structure, assembly mechanism, and integration into functionally distinct intracellular scaffolds. Annu Rev Biochem 73:749–789

Hisanaga S, Hirokawa N (1988) Structure of the peripheral domains revealed by low-angle rotary shadowing. J Mol Biol 202:297–305

Hisanaga S-I, Hirokawa N (1990) Molecular architecture of the neurofilament. II. Reassembly process of neurofilament L protein in vitro. J Mol Biol 211:871–882

Hoffmann PN, Lasek RJ (1975) Slow component of axonal-transport—identification of major structural polypeptides of axon and their generality among mammalian neurons. J Cell Biol 66:351–366

Janmey PA, Leterrier J-F, Herrmann H. (2003) Assembly and structure of neurofilaments. Curr Opin Coll Int Sci 8:40–47

Jones JB, Safinya CR (2008) Interplay between liquid crystalline and isotropic gels in self-assembled neurofilament networks. Biophys J 95:723–835

Kumar S, Yin X, Trapp BD, Hoh JH, Paulatis ME (2002) Relating interactions between neurofilaments to the structure of axonal neurofilament distribution through polymer brush models. Biophys J 82:2360–2372

Kumar S, Hoh JH (2004) Modulation of repulsive forces between neurofilaments by sidearm phosphorylation. Biochem Biophys Res Comm 324:489–496

Lee MK, Xu ZS, Wong PC, Cleveland DW (1993) Neurofilaments are obligate heteropolyemrs in-vivo. J Cell Biol 122:1337–1350

Leermakers FAM, Zhulina EB (2008) Self-consistent field modeling of the neurofilament network. Biophys Rev Lett 3:459–489

Liem RKH, Yen SH, Solomon GD, Shelanski ML (1978) Intermediate filaments in nervous tissues. J Cell Biol 79:637–645

Luchko T, Huzil JT, Stepanova M, Tuszynski J (2008) Conformational analysis of the carboxy-terminal tails of human beta-tubulin isotypes. Biophys J 94:1971–1982

Mitsutake A, Sugita Y, Okamoto Y (2001) Generalized-ensemble algorithms for molecular simulations of biopolymers. Biopolymers 60:96–123

Mukhopadhyay R, Kumar S, Hoh JH (2004) Molecular mechanisms for organizing the neuronal cytoskeleton. BioEssays 26:1–9

Mulligan L, Balin BJ, Lee VMY, Ip W (1991) Antibody labeling of bovine neurofilaments: implications on the structure of neurofilament sidearms. J Struct Biol 166:145–160

Nap RJ, Szleifer I (2008) Structure and interactions of aggrecans: statistical thermodynamic approach. Biophys J 95:4570–4583

Qu LJ, Jin XG, Liao Q (2009) Numerical self-consistent field theory of cylindrical polyelectrolyte brushes. Macromol Theory Simul 18:162–170

Rao MV, Garcia ML, Miyazaki Y, Gotow T, Yuan A, Mattina S, Ward CM, Calcutt NA, Uchiyama Y, Nixon RA, Cleveland D (2002) Gene replacement in mice reveals that the heavily phosphorylated tail of neurofilament heavy subunit does not affect axonal caliber or the transit of cargoes in slow axonal transport. J Cell Biol 158:681–693

Skvortsov AM, Klushin LI, Gorbunov AA (1997) Long and short chains in a polymeric brush: a conformational transition. Macromolecules 30:1818–1827

Skvortsov AM, Klushin LI, Leermakers FAM (2002) Exactly solved polymer models with conformational escape transitions of a coil-to-flower type. Europhys Lett 58:292–298

Sorin EJ, Pande VS (2005) Exploring the helix-coil transition via all-atom equilibrium ensemble simulations. Biophys J 88:2472–2493

Stettler DD, Yamahachi H, Li W, Denk W, Gilbert CD (2006) Axons and synaptic boutons are highly dynamic in adult visual cortex. Neuron 49:877–887

Yuan AD, Rao MV, Sasaki T, Chen Y, Kumar A, Veeranna, Liem RKH, Eyer J, Peterson AC, Julien J-P, Nixon RA (2006) α-internexin is structurally and functionally associated with the

neurofilament triplet proteins in the mature CNS. J Neurosci 26:10006–10019

Zhulina EB, Klein Wolterink J, Borisov OV (2000) Screening effects in polyelectrolyte brush: self-consistent field theory. Macromolecules 33:4945–4953

Zhulina EB, Leermakers FAM (2007) A self-consistent field analysis of the neurofilament brush with amino-acid resolution. Biophys J 93:1431–1441

Zhulina EB, Leermakers FAM (2007) Effect of the ionic strength and pH on the equilibrium structure of neurofilament brush. Biophys J 93:1452–1463

Zhulina EB, Leermakers FAM (2010) The polymer brush model of neurofilament projections. Effect of protein composition. Biophys J 98:462–469